ACS APPLIED MATERIALS & INTERFACES

Research Article

www.acsami.org

Wide-Range Thermometry at Micro/Nano Length Scales with In_2O_3 Octahedrons as Optical Probes

Subrata Senapati and Karuna Kar Nanda*

Materials Research Centre, Indian Institute of Science, Bangalore-560012, India

Supporting Information

ABSTRACT: We report the temperature-dependent photoluminescence and Raman spectra of In_2O_3 octahedrons synthesized by an evaporation−condensation process. The luminescence obtained here is due to the defect-related deep level emission, which shows highly temperature-dependent behavior in 83−573 K range. Both the position as well as the intensity varies with temperature. Similarly, Raman spectroscopy in 83−303 K range shows temperature-dependent variation in peak intensity but no change in the peak position. Interestingly, the variation of intensity for different peaks is consistent with Placzek theory which invokes the possibility of temperature sensing. We demonstrate the reversibility of peak intensity with temperature for consecutive cycles and excellent stability of the octahedrons toward cryogenic temperature sensing. Overall, both the temperature-dependent photoluminescence and Raman spectra can be explored to determine temperature in the cryogenic range at micro/nano length scales. As an example, we evaluate the temperature-dependent Raman spectra of WO_3 that undergoes a phase transition around 210 K and temperature-dependent luminescence of Rhodamine 6G (Rh6G) where intensity varies with temperature.

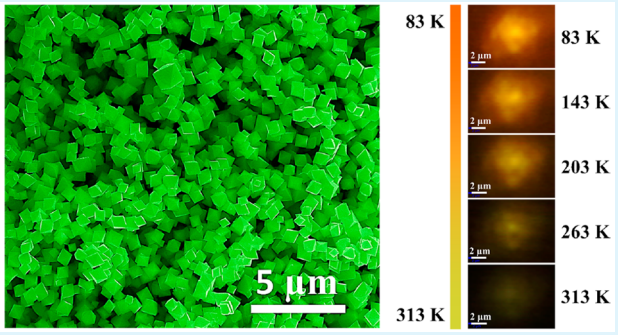

KEYWORDS: *In_2O_3 octahedrons, defect emissions, Raman spectroscopy, optical thermometry, WO_3 phase transition*

INTRODUCTION

In the emerging field of micro/nanotechnology, determination of temperature in micro/nano dimension with high accuracy is a great challenge. When size is reduced to micro/nano dimension, temperature related physical properties of the materials change drastically. Therefore, detection of temperature with submicron resolution is most essential[1−5] especially in the micro and nanoscale optoelectronic devices, living cells, scientific experiments, etc. Various kind of micro/nanothermometers, such as IR thermometers,[6] liquid and solid in tube thermometers,[7,8] nanoscale thermocouples,[9] luminescent thermometers,[10] thermometers based on Raman spectroscopy,[11−13] etc., have been reported for the determination of temperature in submicron scale. Among these nanothermometers, luminescence and Raman spectroscopy based thermometers are widely used due to their own advantages. Determination of temperature can be realized by monitoring the change in luminescence properties such as emission intensities, peak positions, excited state life times, emission band widths,[14,15] etc. in case of luminescence based nanothermometers. Temperature evaluation can be achieved by monitoring the change in Raman intensities, peak shifts, peak widths, etc., in case of Raman spectroscopy based nanothermometers.[11−13,16] For the past three decades or so, various materials, such as organic dyes, quantum dots, micro/nano particles, polymers, phosphors, oxides, etc.,[12−20] have been investigated for luminescence and Raman spectroscopy based thermometers. Because of the high accuracy and sensitivity, these nanothermometers can be used in broad range of applications, such as hot spot measurement in microelectronic circuits, intercellular temperature mapping, detection of temperature of fast moving turbine blades, for samples inside vacuum, in aerodynamic applications,[21−23] etc. Raman spectroscopy based nanothermometers can be used for both solid as well as liquid samples and the availability of Raman active materials is very high. Furthermore, the phase transition associated with temperature can easily be assessed by exploring Raman spectroscopy based thermometers.

In_2O_3 being a wide band gap materials with a direct band gap of 3.6 eV,[24] is widely used for transparent conducting electrode and sensing applications.[25] It emits visible luminescence especially when excited with sub-bandgap excitation because of the presence of different defect states within the band gap.[26] Furthermore, the Raman shift occurs at low frequency for which the temperature-dependency is stronger compared to high frequency. The synthesis of In_2O_3 structures by carbothermal reduction, chemical vapor deposition, thermal evaporation, laser ablation, etc.,[27−29] has also been well documented. Here, we report an evaporation−condensation synthesis of In_2O_3 octahedrons by heating indium metal in air.

Received: June 25, 2015
Accepted: October 8, 2015
Published: October 8, 2015

DOI: 10.1021/acsami.5b05675
ACS Appl. Mater. Interfaces 2015, 7, 23481−23488

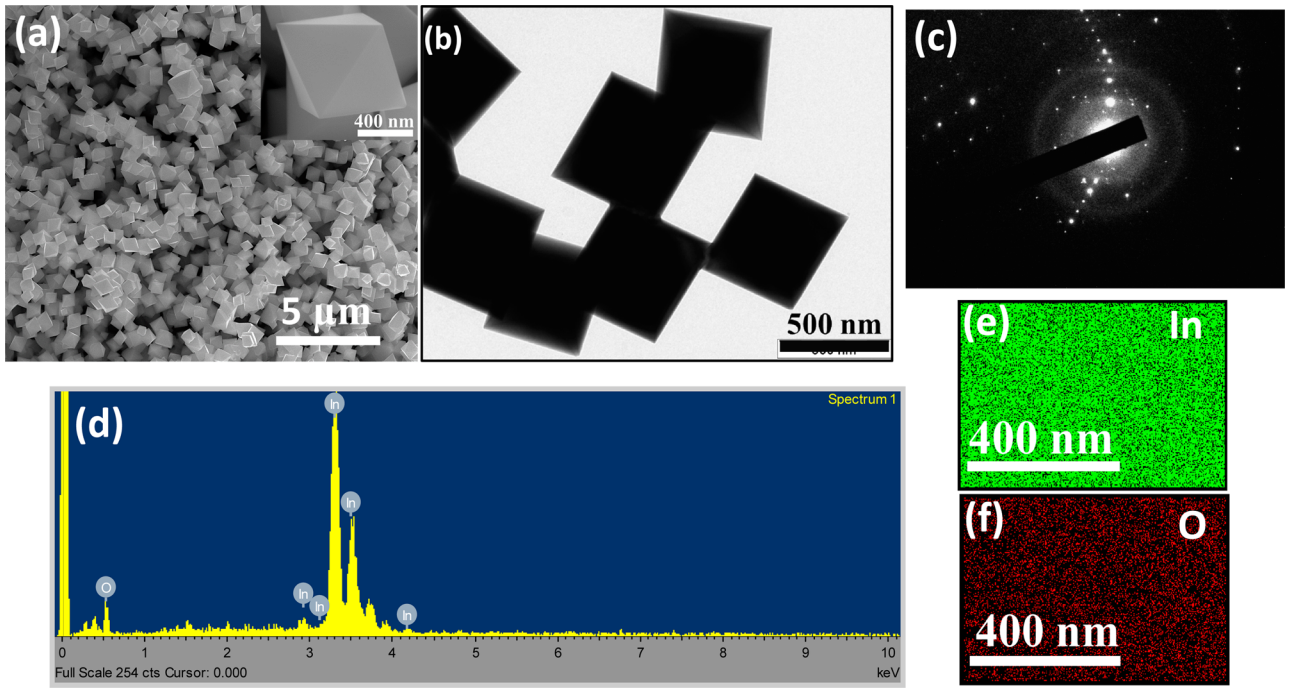

Figure 1. (a) FESEM and (b) TEM images of In_2O_3 octahedrons. Inset of (a) shows a single octahedron. (c) SAED pattern and (d) EDS spectrum of the In_2O_3 octahedrons. (e and f) EDS elemental mapping for In and O, respectively.

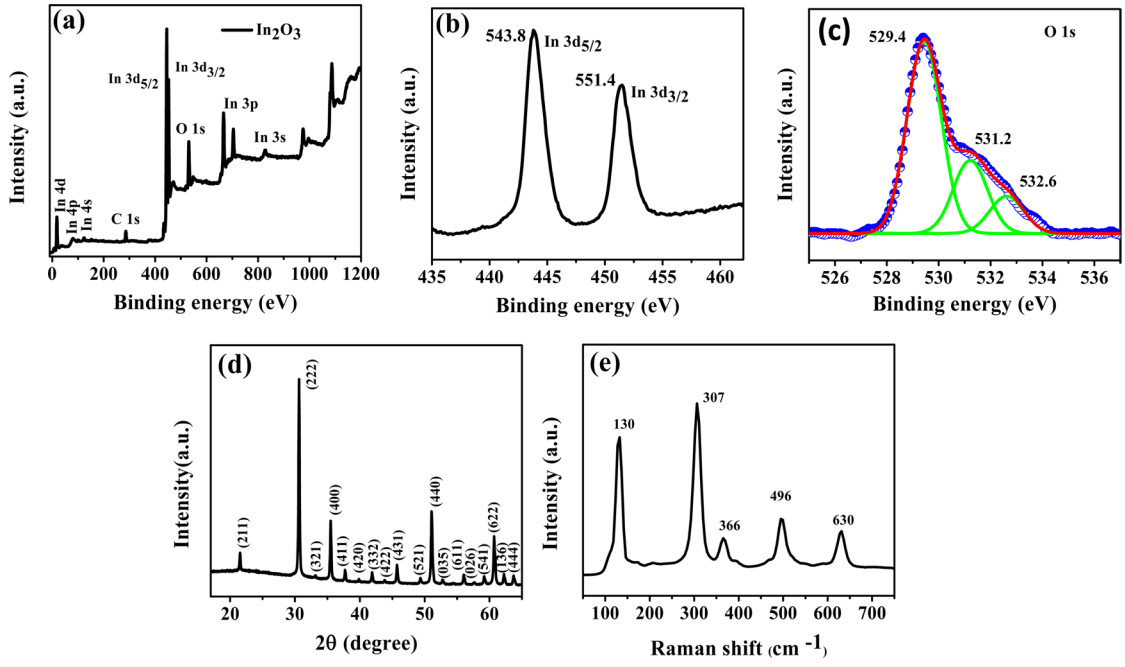

Figure 2. (a) XPS survey spectrum for In_2O_3 octahedrons, (b) XPS spectrum of In, and (c) XPS spectrum of O fitted to three peaks. (d) XRD pattern and (e) Raman spectrum of In_2O_3 octahedrons.

We investigate the temperature-dependent luminescence and Raman spectra of In_2O_3 octahedrons and demonstrate the possibility of temperature sensing. The PL intensity, PL energy, and Raman intensity are explored for temperature sensing in the cryogenic range. As an example, we evaluate the temperature-dependent Raman spectra of WO_3 that undergoes a phase transition at low temperature and temperature-dependent luminescence of Rhodamine 6G (Rh6G).

EXPERIMENTAL SECTION

Synthesis of In_2O_3 octahedrons were carried out in a tube furnace by using indium metal as source material. Indium metal granules (Alfa Aesar, 99.99%, average size 1 mm) were taken in an alumina boat (length 9 cm, width 1 cm) and the boat was placed inside a quartz tube (diameter 2.7 cm) with both ends open. The quartz tube was then inserted into the horizontal tube furnace and the temperature of the furnace was raised to 1200 °C with a heating rate of 20 °C per minute and kept at this temperature for 30 min. The furnace was then allowed to cool down naturally and the In_2O_3 octahedrons were collected in

DOI: 10.1021/acsami.5b05675
ACS Appl. Mater. Interfaces 2015, 7, 23481−23488

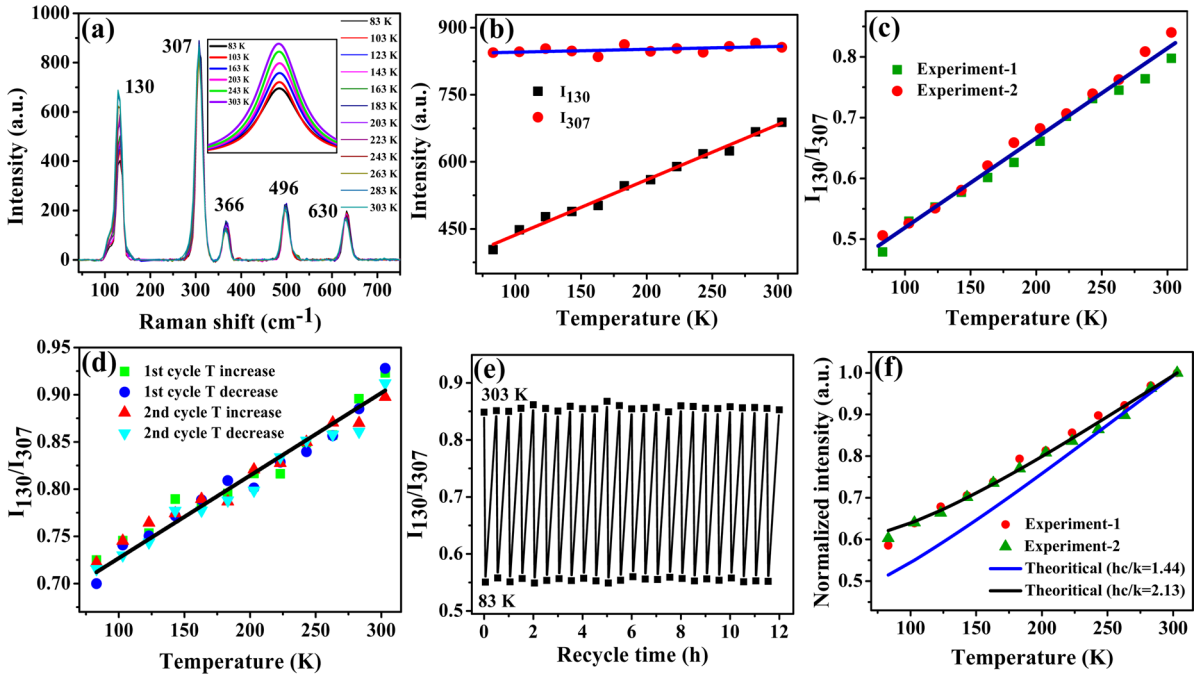

Figure 3. (a) Temperature-dependent Raman spectra of In_2O_3 octahedrons. Inset shows the extended view of 130 cm^{-1} peak for few temperatures, (b) variation of peak intensities (130 and 307 cm^{-1}) with temperature, (c) variation of intensity ratio of two Raman peaks (130 and 307 cm^{-1}) with temperature, (d) intensity ratio of 130 and 307 cm^{-1} peaks for two consecutive cycles, (e) cycle test for intensity ratio of 130 and 307 cm^{-1} peak at 83 and 303 K temperature with 30 min interval, and (f) the normalized intensity as a function of temperature. Experiments 1 and 2 refer to different In_2O_3 octahedrons.

powder form from the boat. The octahedrons were characterized by X-ray diffraction (XRD, PANalytical), field emission scanning electron microscopy (FESEM, FEI Inspect F50), energy dispersive X-ray spectroscopy (EDS, Oxford instrument) attached with FESEM, transmission electron microscopy (TEM, JEM 2100F), X-ray photoelectron spectroscopy (XPS), Raman spectroscopy, and photoluminescence (PL) spectroscopy (WITec 300 with 532 and 355 nm Nd:YAG laser, respectively). The power of 355 nm laser line is 3.5 mW and that of 532 nm line is 12.5 mW. For PL and Raman studies, In_2O_3 octahedrons were dispersed in isopropyl alcohol and drop-casted onto a glass slide and dried under an incandescent bulb (60 °C). The glass slide containing sample was then inserted into a chamber connected to a programmable temperature controlling unit (Linkam) for temperature-dependent studies.

RESULTS AND DISCUSSION

A typical SEM image of as-prepared In_2O_3 octahedrons is shown in Figure 1a. Figure 1b shows the TEM image of In_2O_3 octahedrons. It is evident that eight well faceted equilateral triangles are connected with each other to compose a regular In_2O_3 octahedron, four of which converge to form a nano vertex. The average edge length of each octahedron is ~1.5 μm. All the edges and surfaces of each octahedron are very sharp and smooth indicating no obvious structural defects. Figure 1c shows a diffraction pattern of In_2O_3 which reveals high crystallinity of the octahedrons. EDS spectrum as shown in Figure 1d confirms the presence of Indium and Oxygen and In to O ratio as 0.74 which is greater than the expected ratio 0.67. The EDS elemental mapping is performed on a single In_2O_3 octahedron shown in the inset of Figure 1a and the mapping of Indium and Oxygen is shown in Figure 1e and 1f, respectively. The EDS spectrum and elemental mapping analysis clearly reveal the oxygen deficiency in the In_2O_3 octahedrons. The oxygen deficiency has also been confirmed by XPS studies. Figure 2a shows a typical XPS survey spectrum of In_2O_3 octahedrons. The spectrum confirms the presence of In and O along with carbon. Figure 2b shows the high resolution spectrum of In $3d_{5/2}$ and In $3d_{3/2}$ with peak positions around 443.8 and 551.4 eV, respectively indicating In^{3+} state. The O 1s spectrum as shown in the Figure 2c is deconvoluted into three Gaussian peaks. The peak at 529.4 eV is due to the O^{2-} of the In_2O_3, while the higher energy peaks at 531.2 and 532.6 eV correspond to the oxygen deficiency and surface adsorbed oxygen species,[30,31] respectively. From the XPS data, In to O ratio is found to be 0.77, which is in excellent agreement with that obtained from EDS analysis. The investigation of crystalline phase and structure of In_2O_3 octahedrons is carried out by XRD. Figure 2d shows a typical XRD pattern of octahedrons. All the peaks are indexed to the body centered (bcc) cubic phase of the In_2O_3 with lattice parameter a = 1.012 nm (JCPDS 76−0152).

To investigate further about the phase and structures, Raman spectroscopy of In_2O_3 octahedrons is carried out at room temperature. Figure 2e shows a typical room temperature Raman spectrum of In_2O_3 octahedrons with 532 nm laser excitation. It is well-known that In_2O_3 belongs to cubic bixbyte (also called C-type rare-earth) structures, with space group Ia_3, Th_7.[32] Cubic In_2O_3 consists of 8 formula units in its primitive cell and according to group theory this type of structure should have 120 vibrational modes and can be represented by

$$\Gamma = 4A_g(\mathrm{R}) + 4E_g(\mathrm{R}) + 14T_g(\mathrm{R}) + 5A_u(\mathrm{Inactive}) + 5E_u(\mathrm{Inactive}) + 17T_u(\mathrm{IR}) \quad (1)$$

Among all these vibrational modes, 16 T_u are infrared active and one T_u belongs to acoustic mode, and A_u and E_u are Raman inactive. Only A_g, E_g, and T_g are Raman active and are give rise to total 22 Raman modes.[33−35] It can be noted from Figure 2e

DOI: 10.1021/acsami.5b05675
ACS Appl. Mater. Interfaces 2015, 7, 23481−23488

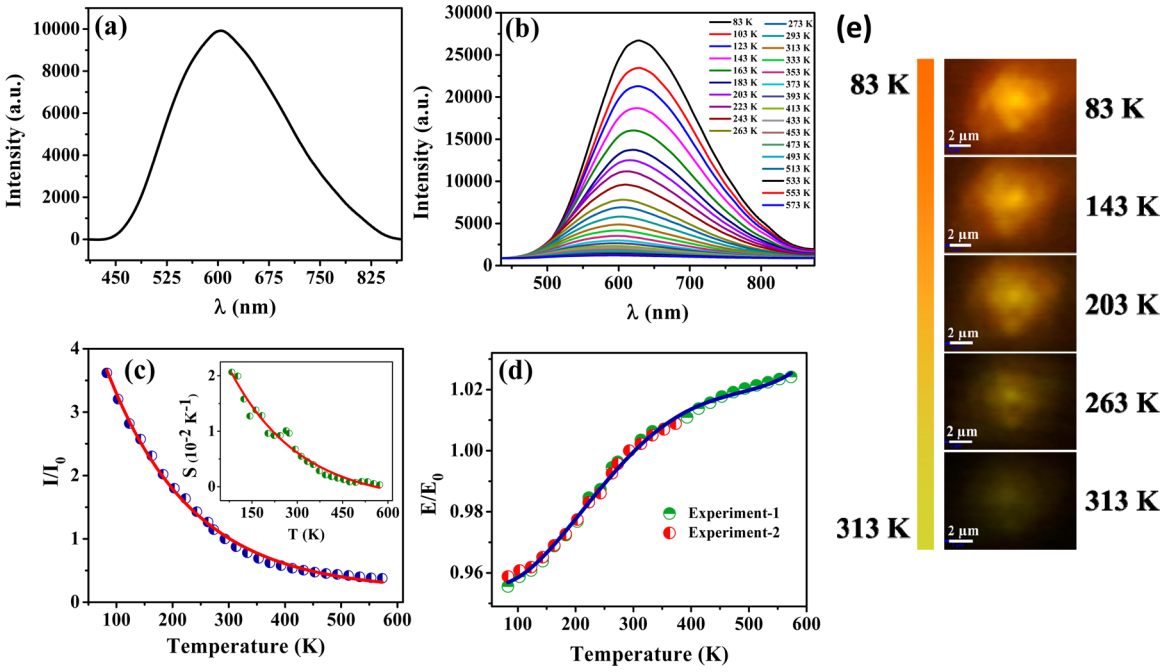

Figure 4. (a) Room-temperature PL spectrum and (b) temperature-dependent PL spectra of In_2O_3 octahedrons. (c) Variation of PL intensity ratio (I/I_0) with temperature, and variation of sensitivity $d(I/I_0)/dT$ as a function of temperature is shown in the inset. (d) Variation of peak energy with temperature. Experiment 1 and 2 refers to different In_2O_3 octahedrons. (e) Optical images of the octahedrons at different temperatures (83−313 K) when exposed to 355 nm.

that five Raman peaks at 130, 307, 366, 496, and 630 cm^{-1} are clearly observed that belong to the vibrational modes of body centered cubic In_2O_3.[36−38] The peak at 130 cm^{-1} is attributed to the vibration of In−O in the InO_6 octahedra unit,[39] the peaks at 307 and 366 cm^{-1} corresponds to the $\delta(InO_6)$ bending vibration, stretching vibrations of In−O−In linkages, respectively and the two peaks at 496 and 630 cm^{-1} are ascribed to the octahedral stretching vibrations $\delta(InO_6)$ of same InO_6 octahedra.[40] To investigate the effect of excitation wavelength, Raman spectrum is also taken with 1064 nm excitation. Figure S1 shows typical room temperature Raman spectra with 532 and 1064 nm of excitation wavelength. The peak at 110 cm^{-1} which appears as a shoulder with 532 nm, is prominent with 1064 nm excitation. This low frequency peak is attributed to the In−O vibration of the InO_6 octahedra unit.[34,39]

Figure 3a shows temperature-dependent Raman spectra of In_2O_3 octahedrons in 83−303 K range with 532 nm excitation. It may be noted that no change in the peak position is observed, while the intensity of 130 and 307 cm^{-1} peaks increases with temperature. Furthermore, the variation of the intensity of 130 cm^{-1} peak is stronger as compared to that of 307 cm^{-1} as shown in Figure 3b. As both the peaks respond differently to temperature, the variation of the intensity ratio can be explored for the determination of temperature. Figure 3c shows the variation of intensity ratio (I_{130}/I_{307}) with temperature for two sets of experiments. The total area under a peak is taken as the intensity value. As shown in Figure 3c, intensity ratio (I_{130}/I_{307}) between Raman peaks at 130 and 307 cm^{-1} shows a linear behavior with temperature. In this context, it may be noted that the linear behavior of the measurable quantity with temperature is one of the most essential requirements for temperature sensing and the calculation of sensitivity of the sensor. Generally, the sensitivity S and the relative sensitivity S_R are given by

$$S = dX/dT \text{ and } S_R = S/X$$

where X is the intensity ratio between two Raman peaks and T is the absolute temperature. From Figure 3c, the sensitivity is found to be 1.7×10^{-3} K^{-1} which is almost constant throughout the temperature range (83−303 K) and is comparable to the reported values (Table S1). However, the relative sensitivity varies with temperature (Figure S2a) and the maximum S_R is found to be 3.6×10^{-3} at 83 K. It may be noted here that absolute change in intensity is more useful rather than relative change for practical application point of view and the sensitivity is more meaningful. The accuracy in the measurement is found to be ±0.2 K.

For any kind of sensors, reproducibility and stability are the most essential requirements for better performance and longevity of the sensor. In order to test the reproducibility, we perform two consecutive temperature cycles studies in 83−303 K range with 20 K temperature difference. The intensity ratio between 130 and 307 cm^{-1} as shown in Figure 3d remains almost linear with temperature in each half cycle (one-half cycle represents 83 to 303 K, other one represents 303 to 83 K) and is reversible by continuous heating and cooling cycle, which shows the reproducibility of the sensor material. Hysteresis curves for two consecutive heating and cooling cycles as shown in Figure S3 reveals almost no hysteresis. The stability or longevity of the sensor is tested by 12 h cycle test. The intensity ratio is obtained at 83 and 303 K with 30 min interval without disturbing the sample position. The intensity ratio remains the same in the entire test range as shown in Figure 3e indicating high stability of the octahedrons as sensing materials. This indicates that the In_2O_3 octahedrons qualify as cryogenic temperature probe. It is our belief that nanosize In_2O_3 can also be used for the same.

Here it is ascertained that the variation of Raman peak intensity of 130 cm^{-1} peak with temperature is stronger as

DOI: 10.1021/acsami.5b05675
ACS Appl. Mater. Interfaces 2015, 7, 23481−23488

compared to other peaks. According to the Placzek theory (quantum mechanical model), intensity of Raman peaks and temperature can be related as[41]

$$I \approx (\hbar/2\omega_{\mu}) \times (\omega_0 - \omega_{\mu})^4[1 + (\exp(hc\omega_{\mu}/kT) - 1)^{-1}] \quad (2)$$

where I is the intensity of Raman peak, ω_0 is frequency (cm^{-1}) of the excitation source, ω_{μ} is the Raman shift (cm^{-1}) of the peak, T is the temperature in K, and other symbols have their usual meanings. As ω_0 is constant for all Raman peaks, the intensity of different peaks depends on ω_{μ} and temperature. On the basis of eq 2, the intensity as a function of temperature is computed and shown in Figure S4 for different ω_{μ}. It is evident from Figure S4 that the variation of 130 cm^{-1} peak is stronger as compared to 370 cm^{-1} one and the intensity is almost independent of temperature for larger frequency shift. Overall, the experimental results are consistent with the theoretical one. It can be noted from eq 2 that the normalized intensity depends only on temperature. The normalized intensity of 130 cm^{-1} peak as a function of temperature is shown in Figure 3f. It is evident that both the experimental as well as the theoretical results are consistent with each other in the entire range studied. Though the theoretical value of hc/k is 1.44, a value of 2.13 which is ~3/2 times of 1.44, reproduces the experimental data reasonably. It is, therefore, suggested further theoretical insight into account for the discrepancy.

Apart from ratiometric sensing discussed earlier, temperature sensing can be realized using normalized peak intensity as well. Figure 3f shows the normalized 130 cm^{-1} peak intensity variation with temperature. Sensitivity is found to be 1.9×10^{-3} K^{-1} which is almost constant in the range 83−303 K, while the relative sensitivity varies with temperature (Figure S2b) and the maximum S_R is 3.1×10^{-3} at 83 K. The accuracy in the measurement is ±0.3 K.

Now, we report the PL of In_2O_3 octahedrons on glass substrates. Generally, UV emission due to the electronic transition between valence band (VB) and conduction band (CB), called near band edge (NBE) emission and other the visible emission, due to different defects or trap states mediated deep level (DL) emission,[42] are expected for In_2O_3. Figure 4a shows a typical room temperature PL spectrum of In_2O_3 octahedrons with 355 nm laser as source of excitation. As the excitation energy is lower than the band gap energy of In_2O_3, no NBE emission is seen. However, a highly intense yellowish orange emission with peak centered around 605 nm is apparent. It is well-known that bulk In_2O_3 does not emit any visible luminescence at room temperature.[43] When the size is reduced to micro/nano dimensions, the emission arises because of the quantum confinement effect[44,45] and several defects presence in materials.[46] Because of the size of the In_2O_3 octahedrons is too large to observe quantum confinement effect (the critical Bohr radius for In_2O_3 is about 2.14 nm),[47] the effect of quantum confinement is not applicable in our case. The emission obtained in the visible range is due to the presence of defects. The PL emission from various morphologies of In_2O_3 nano/micro structures in the whole visible region starting from 400 to 650 nm have been reported.[48−51] All the emissions are ascribed to be due to the presence of different defects. The common defects are oxygen vacancy, indium vacancy, oxygen interstitials, indium interstitials, staking faults, etc.[49] As the In_2O_3 octahedrons are synthesized by high temperature evaporation−condensation process, which may leads to the formation of various defects such as oxygen vacancy, indium interstitials, stacking faults, etc. Presence of oxygen deficiency is well supported by the EDS and XPS analyses. All these defect bands act as donor levels within the energy gap. The radiative recombination between electrons in the donor levels and the photo excited holes in the VB give rise to the emission in the visible region.[52] A typical band diagram for In_2O_3 is shown in Figure S5, which gives the idea about presence of different defect states within the energy gap that are responsible for luminescence.

To study the effect of temperature, temperature-dependent PL studies of In_2O_3 octahedrons are implemented in the range of 83−573 K. Figure 4b shows the PL spectra obtained at various temperatures. It may be noted that the peak intensity decreases accompanied by a blue shift in peak position with increase in temperature. Figure 4c shows the variation of intensity ratio (I/I_0) with temperature, where I is the integrated intensity at various temperature and I_0 is the integrated intensity at room temperature. The variation of intensity ratio with temperature is used to evaluate sensitivity and the sensitivity $d(I/I_0)/dT$ as a function of temperature is shown in the inset of Figure 4c. The sensitivity increases as the temperature is decreased and the maximum sensitivity is 2.1×10^{-2} K^{-1} at 83 K. The relative sensitivity also varies with temperature as shown in Figure S6a and the maximum relative sensitivity is 8.4×10^{-3} at 273 K with an accuracy of ±0.6 K. The sensitivity is found to be superior as compared to other materials reported in literature (Table S1). It may be noted here that the variation of peak position with temperature can also be explored for temperature sensing. Variation of peak position (E/E_0) with temperature for two sets of experiments is shown in Figure 4d, where E is the peak energy at different temperature and E_0 is the peak energy at room temperature. The maximum sensitivity $d(E/E_0)/dT$ is 3.2×10^{-4} K^{-1} at 203 K and maximum relative sensitivity (Figure S6b) is 3.3×10^{-4} at 203 K with an accuracy of ±3.0 K. For comparison with reported sensitivity, variation of E with temperature is plotted in Figure S7. Maximum sensitivity is found to be 6.3×10^{-4} K^{-1}, which is comparable with reported values (Table S2) with an accuracy of ±3.0 K. Over all, the results suggest that the octahedrons are better suited for low temperature sensing.

Optical images of the octahedrons at different temperatures (83−313 K) when exposed to 355 nm excitation are shown in Figure 4e. It is apparent that the intensity as well the color of luminescence depends on the temperature and is in accordance with the luminescence spectra. It depicts orange emission at 83 K and yellowish color with decrease in intensity at 313 K.

Now, we understand the variation of luminescence intensity with temperature. At higher temperature, electron−phonon interaction dominates over electron−hole interactions that favor nonradiative recombination which lowers the number of emitted photons and hence, the emission intensity. On the other hand, the number of phonon is less at low temperature which favors the radiative recombination and hence, the enhancement in the emission intensity. Overall, the PL emission intensity is highest at 83 K and intensity decreases exponentially with increase of temperature from 83 to 573 K. Along with decrease in PL intensity, a blue-shift in the peak position is clearly observed with increase in temperature. It may be noted that the emission observed for In_2O_3 octahedrons is due to defect states and the electron population in defect states depends on temperature. With increase of temperature, defect states with higher energy become more active that causes the increase in separation between electrons and holes recombina-

DOI: 10.1021/acsami.5b05675
ACS Appl. Mater. Interfaces 2015, 7, 23481−23488

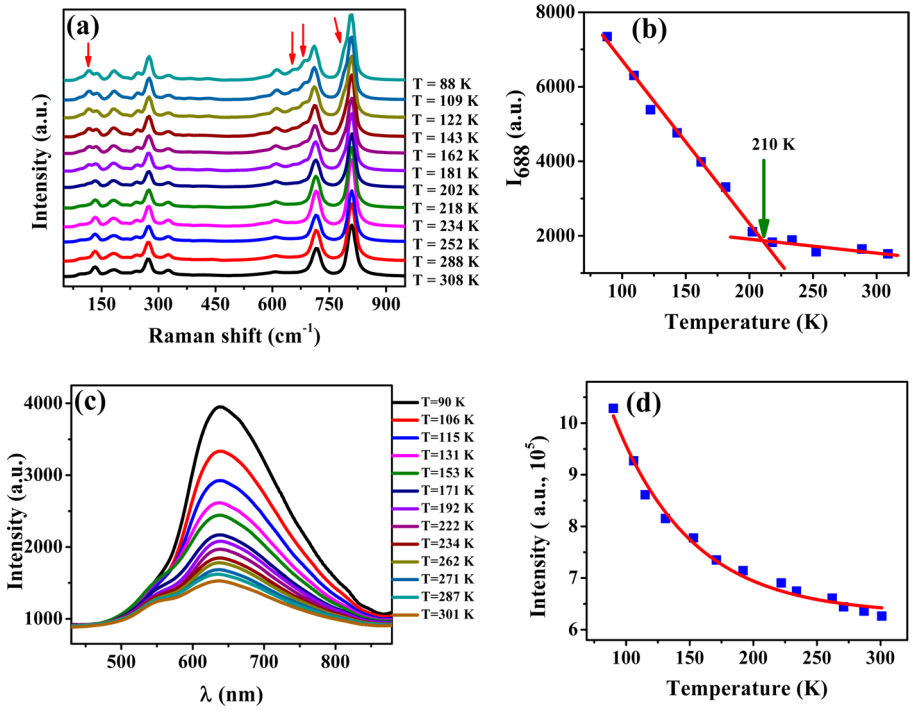

Figure 5. (a) Temperature-dependent Raman spectra of WO_3 with temperature, arrows indicate the appearance of N-phase, (b) variation of Raman peak (688 cm^{-1}) with temperature, (c) temperature-dependent PL spectra of Rh6G, and (d) variation of integrated PL intensity of Rh6G with temperature.

tion path and a blue-shift in emission peak is observed.[53,54] In general, the temperature induced lattice expansion causes decrease in energy gap and red-shift is observed. No change in Raman peak frequency suggest that the bond between In and O is strong that lattice expansion is too small. Overall, blue-shift in peak energy is observed due to the defect state population.

We also carried out similar studies on silicon substrates and highly compressed pellet of In_2O_3. It is evident from Figures S8–S11 that the PL results are almost independent (Table S3). We also investigate the temperature-dependent PL of annealed In_2O_3. The as-prepared In_2O_3 is annealed at 1200 and 1300 °C in oxygen atmosphere. Temperature dependent PL, variation of emission intensity and peak energy with temperature is given in Figure S12. The sensitivity (Table S3) obtained for annealed In_2O_3 is on the order of 10^{-1}, which is higher compared to that of as-prepared In_2O_3 but the operating range reduces to 83–313 K.

It is known that WO_3 remains in monoclinic γ-phase at room temperature and undergoes a phase transition around 200 K to a new N-phase.[55,56] To probe the temperature and study the phase transition, Raman studies are carried out on In_2O_3 and WO_3 by placing both the samples side by side. Figure 5a shows the temperature-dependent Raman spectra of WO_3 sample. It may be noted here that the temperature indicated against each spectrum is obtained from normalized peak intensity (130 cm^{-1}) of In_2O_3. The Raman spectra reveal the existence of both N-phase and γ- phase below 218 K. The peaks at 96, 132, 183, 214, 240, 273, 325, 374, 434, 611, 717, and 807 cm^{-1} correspond to γ-phase and the peaks at 117, 658, 687, and 789 cm^{-1} (marked by arrows) correspond to N-phase. To evaluate the transition temperature, the variation of intensity of 687 cm^{-1} peak is plotted as a function of temperature and shown in Figure 5b. A transition temperature of ~210 K is evaluated which is consistent with earlier reports.[55,56]

We also probe the temperature-dependent PL intensity of Rhodamine 6G (Rh6G) by using In_2O_3 as luminescent probe. First of all, we deduce the temperature from energy versus temperature data and then record the PL spectra for Rh6G. The temperature-dependent PL spectra of Rh6G are shown in Figure 5c and the variation of PL intensity with temperature is shown in Figure 5d. It is observed that the intensity of Rh6G decreases monotonically with increase of temperature which is consistent with earlier reports.[57,58]

CONCLUSION

In conclusion, we report the evaporation–condensation synthesis and temperature-dependent optical properties of In_2O_3 octahedrons. Furthermore, we show that the optical properties can be explored for temperature sensing in 83–573 K range. The temperature sensing is possible by two different methods using the same In_2O_3 octahedrons: one is luminescence based and the other is by Raman spectroscopy based sensing. The defects related emission obtained from In_2O_3 octahedrons shows highly temperature-dependent behavior. Both the luminescence intensity/peak position varies with temperature which can be used for luminescence based temperature sensing. On the other hand, the intensity of Raman peaks varies with temperature while the position does not change. Interestingly, the intensity of different peaks varies differently with temperature. The variation of intensity ratio between two peaks is linear with temperature which is very much advantageous for temperature sensing. Furthermore, the stability and the reversibility of sensor are excellent which indicate the In_2O_3 octahedrons qualify as optical probe for temperature sensing. As an example, the phase transition of WO_3 around 210 K is demonstrated by Raman measurement and the monotonic decrease of PL intensity with temperature for Rh6G is demonstrated. Overall, our results demonstrate the

DOI: 10.1021/acsami.5b05675
ACS Appl. Mater. Interfaces 2015, 7, 23481–23488

proof-of-concept that can be used in cryogenic thermometry irrespective of the size of the crystallites. Also, the work is expected to motivate researchers to develop materials for accurate and versatile temperature sensing.

■ ASSOCIATED CONTENT

Supporting Information

The Supporting Information is available free of charge on the ACS Publications website at DOI: 10.1021/acsami.5b05675.

Raman spectra at two different laser lines, relative sensitivity variation with temperature, hysteresis curve, theoretical variation of Raman intensities with temperature, band diagram of In_2O_3, variation of peak energy with temperature, room-temperature and temperature-dependent PL of In_2O_3 at Si substrate, temperature-dependent PL of In_2O_3 pellet, room-temperature and temperature-dependent PL of In_2O_3 sample annealed at different temperatures, comparison tables for sensitivity of intensity and peak shift based sensing, and comparison of sensitivity of temperature-dependent PL of In_2O_3 sample at various conditions. (PDF)

■ AUTHOR INFORMATION

Corresponding Author

*Phone: +91-080-2293 2996. Fax: +91-80-2360 7316. E-mail: nanda@mrc.iisc.ernet.in.

Author Contributions

All authors were involved in the work and in writing the manuscript. S.S. synthesized and characterized the samples.

Notes

The authors declare no competing financial interest.

■ ACKNOWLEDGMENTS

The authors acknowledge the financial assistance from DST through the Nanomission.

■ REFERENCES

(1) Kucsko, G.; Maurer, P. C.; Yao, N. Y.; Kubo, M.; Noh, H. J.; Lo, P. K.; Park, H.; Lukin, M. D. Nanometre-scale Thermometry in a Living Cell. *Nature* **2013**, *500*, 54−58.

(2) Guo, H.; Khan, M. I.; Cheng, C.; Fan, W.; Dames, C.; Wu, J.; Minor, A. M. Vanadium Dioxide Nanowire-based Microthermometer for Quantitative Evaluation of Electron Beam Heating. *Nat. Commun.* **2014**, *5*, 4986.

(3) Lee, J.; Kotov, N. A. Thermometer Design at the Nanoscale. *Nano Today* **2007**, *2*, 48−51.

(4) Brites, C. D. S.; Lima, P. P.; Silva, N. J. O.; Millan, A.; Amaral, V. S.; Palacio, F.; Carlos, L. D. Thermometry at the Nanoscale. *Nanoscale* **2012**, *4*, 4799−4829.

(5) Sadat, S.; Tan, A.; Chua, Y. J.; Reddy, P. Nanoscale Thermometry Using Point Contact Thermocouples. *Nano Lett.* **2010**, *10*, 2613−2617.

(6) Cerruti, M. G.; Sauthier, M.; Leonard, D.; Liu, D.; Duscher, G.; Feldheim, D. L.; Franzen, S. Gold and Silica-coated Gold Nanoparticles as Thermographic Labels for DNA Detection. *Anal. Chem.* **2006**, *78*, 3282−3288.

(7) Gao, Y. H.; Bando, Y.; Liu, Z. W.; Golberg, D.; Nakanishi, H. Temperature Measurement Using a Gallium-filled Carbon Nanotube Nanothermometer. *Appl. Phys. Lett.* **2003**, *83*, 2913−2915.

(8) Wang, C. Y.; Gong, N. W.; Chen, L. J. High-sensitivity Solid-state Pb(core)/ZnO(shell) Nanothermometers Fabricated by a Facile Galvanic Displacement Method. *Adv. Mater.* **2008**, *20*, 4789−4792.

(9) Aigouy, L.; Tessier, G.; Mortier, M.; Charlot, B. Scanning Thermal Imaging of Microelectronic Circuits with a Fluorescent Nanoprobe. *Appl. Phys. Lett.* **2005**, *87*, 184105.

(10) Ye, F.; Wu, C.; Jin, Y.; Chan, Y. H.; Zhang, X.; Chiu, D. T. Ratiometric Temperature Sensing with Semiconducting Polymer Dots. *J. Am. Chem. Soc.* **2011**, *133*, 8146−8149.

(11) Song, L.; Ma, W.; Ren, Y.; Zhou, W.; Xie, S.; Tan, P.; Sun, L. Temperature Dependence of Raman Spectra in Single-walled Carbon Nanotube Rings. *Appl. Phys. Lett.* **2008**, *92*, 121905.

(12) Calizo, I.; Balandin, A.; Bao, W.; Miao, F.; Lau, C. Temperature Dependence of the Raman Spectra of Graphene and Graphene Multilayers. *Nano Lett.* **2007**, *7*, 2645−2649.

(13) Spindler, M.; Uhlig, B.; Menzel, S. B.; Huck, C.; Gemming, T.; Eckert, J. Local Temperature Determination in Power Loaded Surface Acoustic Wave Structures Using Raman Spectroscopy. *J. Appl. Phys.* **2013**, *114*, 164317.

(14) Jaque, D.; Vetrone, F. Luminescence Nanothermometry. *Nanoscale* **2012**, *4*, 4301−4326.

(15) Shinde, S. L.; Nanda, K. K. Wide-range Temperature Sensing Using Highly Sensitive Green Luminescent ZnO and PMMA-ZnO Film as a Non-contact Optical Probe. *Angew. Chem., Int. Ed.* **2013**, *52*, 11325−11328.

(16) Yue, Y.; Wang, X. Nanoscale Thermal Probing. *Nano Rev.* **2012**, *3*, 11586.

(17) Wawrzynczyk, D.; Bednarkiewicz, A.; Nyk, M.; Strek, W.; Samoc, M. Neodymium(III) Doped Fluoride Nanoparticles as Non-contact Optical Temperature Sensors. *Nanoscale* **2012**, *4*, 6959−6961.

(18) Aigouy, L.; Tessier, G.; Mortier, M.; Charlot, B. Scanning Thermal Imaging of Microelectronic Circuits with a Fluorescent Nanoprobe. *Appl. Phys. Lett.* **2005**, *87*, 184105.

(19) Okabe, K.; Inada, N.; Gota, C.; Harada, Y.; Funatsu, T.; Uchiyama, S. Intracellular Temperature Mapping with a Fluorescent Polymeric Thermometer and Fluorescence Lifetime Imaging Microscopy. *Nat. Commun.* **2012**, *3*, 705.

(20) Borisov, S. M.; Gatterer, K.; Bitschnau, B.; Klimant, I. Preparation and Characterization of Chromium(III)-activated Yttrium Aluminum Borate: A New Thermographic Phosphor for Optical Sensing and Imaging at Ambient Temperatures. *J. Phys. Chem. C* **2010**, *114*, 9118−9124.

(21) Wang, X.; Kong, X. G.; Yu, Y.; Sun, Y. J.; Zhang, H. Effect of Annealing on Upconversion Luminescence of ZnO:Er^{3+} Nanocrystals and High Thermal Sensitivity. *J. Phys. Chem. C* **2007**, *111*, 15119−15124.

(22) Khalid, A. H.; Kontis, K. 2D Surface Thermal Imaging Using Rise-time Analysis From Laser-induced Luminescence Phosphor Thermometry. *Meas. Sci. Technol.* **2009**, *20*, 025305.

(23) Singh, S. K.; Kumar, K.; Rai, S. B. Er^{3+}/Yb^{3+} Codoped Gd_2O_3 Nano-phosphor for Optical Thermometry. *Sens. Actuators, A* **2009**, *149*, 16−20.

(24) Wu, P.; Li, Q.; Zhao, C. X.; Zhang, D. L.; Chi, L. F.; Xiao, C. T. Synthesis and Photoluminescence Property of Indium Oxide Nanowires. *Appl. Surf. Sci.* **2008**, *255*, 3201−3204.

(25) Wang, C.; Chen, D.; Jiao, X. Flower-like In_2O_3 Nanostructures Derived from Novel Precursor: Synthesis, Characterization, and Formation Mechanism. *J. Phys. Chem. C* **2009**, *113*, 7714−7718.

(26) Jean, S. T.; Her, Y. C. Growth Mechanism and Photoluminescence Properties of In_2O_3 Nanotowers. *Cryst. Growth Des.* **2010**, *10*, 2104−2110.

(27) Qurashi, A.; El-Maghraby, E. M.; Yamazaki, T.; Kikuta, T. J. Catalyst-free Shape Controlled Synthesis of In_2O_3 Pyramids and Octahedron: Structural Properties and Growth Mechanism. *J. Alloys Compd.* **2009**, *480*, L9−L12.

(28) Jia, H.; Zhang, Y.; Chen, X.; Shu, J.; Luo, X.; Zhang, Z.; Yu, D. Efficient Field Emission from Single Crystalline Indium Oxide Pyramids. *Appl. Phys. Lett.* **2003**, *82*, 4146−4148.

(29) Guha, P.; Kar, S.; Chaudhuri, S. Direct Synthesis of Single Crystalline In_2O_3 Nanopyramids and Nanocolumns and Their Photoluminescence Properties. *Appl. Phys. Lett.* **2004**, *85*, 3851−3853.

DOI: 10.1021/acsami.5b05675
ACS Appl. Mater. Interfaces 2015, 7, 23481−23488

(30) Luo, S.; Zhou, W.; Zhang, Z.; Shen, J.; Liu, L.; Ma, W.; Zhao, X.; Liu, D.; Song, L.; Xiang, Y.; Zhou, J.; Xie, S.; Chu, W. Conformal Conversion from Helical Hexagonal InN Microtubes to In_2O_3 Counterparts. *Appl. Phys. Lett.* **2006**, *89*, 093112.
(31) Kim, W. J.; Pradhan, D.; Sohn, Y. Fundamental Nature and CO Oxidation Activities of Indium Oxide Nanostructures: 1D-wires, 2D-plates, and 3D-cubes and donuts. *J. Mater. Chem. A* **2013**, *1*, 10193−10202.
(32) White, W. B.; Keramidas, V. G. Vibrational Spectra of Oxides with the C-type Rare Earth Oxide Structure. *Spectrochim. Acta, Part A* **1972**, *28*, 501−509.
(33) Garcia- Domene, B.; Ortiz, H. M.; Gomis, O.; Sans, J. A.; Manjón, F. J.; Muñoz, A.; Hernández, P. R.; Achary, S. N.; Errandonea, D.; García, D. M.; Romero, A. H.; Singhal, A.; Tyagi, A. K. High-pressure Lattice Dynamical Study of Bulk and Nanocrystalline In_2O_3. *J. Appl. Phys.* **2012**, *112*, 123511.
(34) Wang, C. Y.; Dai, Y.; Pezoldt, J.; Lu, B.; Kups, T.; Cimalla, V.; Ambacher, O. Phase Stabilization and Phonon Properties of Single Crystalline Rhombohedral Indium Oxide. *Cryst. Growth Des.* **2008**, *8*, 1257−1260.
(35) Berengue, O. M.; Lanfredi, A. J. C.; Pozzi, L. P.; Rey, J. F. Q.; Leite, E. R.; Chiquito, A. J. Magnetoresistance in Sn-doped In_2O_3 Nanowires. *Nanoscale Res. Lett.* **2009**, *4*, 921−925.
(36) Ren, W.; Liu, Y.; Mei, Z.; Wen, X.; Wang, S. $In(OH)_3$ and In_2O_3 Nanorice and Microflowers: Morphology Transformation and Optical Properties. *J. Nanopart. Res.* **2013**, *15*, 1452.
(37) Gali, P.; Sapkota, G.; Syllaios, A. J.; Littler, C.; Philipose, U. Stoichiometry Dependent Electron Transport and Gas Sensing Properties of Indium Oxide Nanowires. *Nanotechnology* **2013**, *24*, 225704.
(38) Seetha, M.; Meena, P.; Mangalaraj, D.; Masuda, Y.; Senthil, K. Synthesis of Indium Oxide Cubic Crystals by Modified Hydrothermal Route for Application in Room Temperature Flexible Ethanol Sensors. *Mater. Chem. Phys.* **2012**, *133*, 47−54.
(39) Gan, J.; Lu, X.; Wu, J.; Xie, S.; Zhai, T.; Yu, M.; Zhang, Z.; Mao, Y.; Wang, S. C.; Shen, Y.; Tong, Y. Oxygen Vacancies Promoting Photoelectrochemical Performance of In_2O_3 Nanocubes. *Sci. Rep.* **2013**, *3*, 1021.
(40) Elouali, S.; Bloor, L. G.; Binions, R.; Parkin, I. P.; Carmalt, C. J.; Darr, J. A. Gas Sensing with Nano-Indium Oxides (In_2O_3) Prepared via Continuous Hydrothermal Flow Synthesis. *Langmuir* **2012**, *28*, 1879−1885.
(41) Herchen, H.; Cappelli, M. A. First-order Raman Spectrum of Diamond at High Temperatures. *Phys. Rev. B: Condens. Matter Mater. Phys.* **1991**, *43*, 11740−11744.
(42) Shi, M.; Xu, F.; Yu, K.; Zhu, Z.; Fang, J. Controllable Synthesis of In_2O_3 Nanocubes, Truncated Nanocubes, and Symmetric Multipods. *J. Phys. Chem. C* **2007**, *111*, 16267−16271.
(43) Ohhata, Y.; Shinoki, F.; Yoshida, S. Optical Properties of R.F. Reactive Sputtered Tin-doped In_2O_3 Films. *Thin Solid Films* **1979**, *59*, 255−261.
(44) Zeng, F.; Zhang, X.; Wang, J.; Wang, L.; Zhang, L. Large-scale Growth of In_2O_3 Nanowires and Their Optical Properties. *Nanotechnology* **2004**, *15*, 596−600.
(45) Liang, C. H.; Meng, G. W.; Lei, Y.; Phillipp, F.; Zhang, L. D. Catalytic Growth of Semiconducting In_2O_3 Nanofibers. *Adv. Mater.* **2001**, *13*, 1330−1333.
(46) Kumar, M.; Singh, V. N.; Singh, F.; Lakshmi, K. V.; Mehta, B. R.; Singh, J. P. On the Origin of Photoluminescence in Indium Ixide Octahedron Structures. *Appl. Phys. Lett.* **2008**, *92*, 171907.
(47) Peng, X. S.; Meng, G. W.; Zhang, J.; Wang, X. F.; Wang, Y. W.; Wang, C. Z.; Zhang, L. D. Synthesis and Photoluminescence of Single-crystalline In_2O_3 Nanowires. *J. Mater. Chem.* **2002**, *12*, 1602−1605.
(48) Mazzera, M.; Zha, M.; Calestani, D.; Zappettini, A.; Salviati, G.; Zanotti, L. Low-temperature In_2O_3 Nanowire Luminescence Properties as a Function of Oxidizing Thermal Treatments. *Nanotechnology* **2007**, *18*, 355707.
(49) Tomita, T.; Yamashita, K.; Hayafuji, Y.; Adachi, H. The Origin of n-type Conductivity in Undoped In_2O_3. *Appl. Phys. Lett.* **2005**, *87*, 051911.
(50) Wang, C.; Chen, D.; Jiao, X.; Chen, C. Lotus-root-like In_2O_3 Nanostructures: Fabrication, Characterization, and Photoluminescence Properties. *J. Phys. Chem. C* **2007**, *111*, 13398−13403.
(51) Cao, H.; Qiu, X.; Liang, Y.; Zhu, Q.; Zhao, M. Room-temperature Ultraviolet-emitting In_2O_3 Nanowires. *Appl. Phys. Lett.* **2003**, *83*, 761−763.
(52) Gao, T.; Wang, T. Catalytic Growth of In_2O_3 Nanobelts by Vapor Transport. *J. Cryst. Growth* **2006**, *290*, 660−664.
(53) Chen, L. C.; Tien, C. H.; Liao, W. C. A phosphor-free White Light-emitting Diode Using In_2O_3:Tb Transparent Conductive Light Converter. *J. Phys. D: Appl. Phys.* **2011**, *44*, 165101.
(54) Ho, C. H.; Chan, C. H.; Tien, L. C.; Huang, Y. S. Direct Optical Observation of Band-edge Excitons, Band Gap, and Fermi Level in Degenerate Semiconducting Oxide Nanowires In_2O_3. *J. Phys. Chem. C* **2011**, *115*, 25088−25096.
(55) Cazzanelli, E.; Vinegoni, C.; Mariotto, G.; Kuzmin, A.; Purans, J. Low-temperature Polymorphism in Tungsten Trioxide Powders and Its Dependence on Mechanical Treatments. *J. Solid State Chem.* **1999**, *143*, 24−32.
(56) Souza, A. G.; Mendes, J.; Freire, V. N.; Ayala, A. P.; Sasaki, J. M.; Freire, P. T. C.; Melo, F. E. A.; Juliao, J. F.; Gomes, U. U. Phase Transition in WO_3 Microcrystals Obtained by Sintering Process. *J. Raman Spectrosc.* **2001**, *32*, 695−699.
(57) Yeshchenko, O. A.; Bondarchuk, I. S.; Kozachenko, V. V.; Losytskyy, M. Yu. Surface Plasmon Enhanced Photoluminescence of Rhodamine 6G on Au Nanoparticles 2D Array: Temperature Effects. *Proc. Int. Conf. Nanomater.: Appl. and Prop.* **2014**, *3*, 02MAN04.
(58) Dwivedi, Y.; Rai, S. B.; Thakur, S. N. Optical Properties of Rh 6G Dye in Liquid and Solid Polymer. *Spectrochim. Acta, Part A* **2008**, *69*, 789−793.

DOI: 10.1021/acsami.5b05675
ACS Appl. Mater. Interfaces 2015, 7, 23481−23488